

Achieving highly practical capacitance of MnO₂ by using chain-like CoB alloy as support

Jingjing Yan,^a Hui Wang,^a Shan Ji,^{b*} Bruno G Pollet,^c and Rongfang Wang,^{a**}

^a Institute of Chemical Engineering, Qingdao University of Science and Technology,
Qingdao, 266042, China

^b College of Biological, Chemical Science and Chemical Engineering, Jiaying
University, Jiaying, 314001, China

^c Department of Energy and Process Engineering, Faculty of Engineering, Norwegian
University of Science and Technology (NTNU), NO-7491 Trondheim, Norway

Corresponding authors:

Shan Ji (*): jssshan@126.com, Tel./fax: +86 (0)15024355548

Rongfang Wang (**): wrf38745779@126.com, Tel./fax: +86-931-7971533

Abstract:

The practical performance of MnO₂ as a capacitor material is limited mainly by its poor electronic conductivity. Arranging MnO₂ on the conductive backbone to form a unique hierarchical nanostructure is an efficient way to enhance its capacitor performance. Herein, a hierarchically core-shell structure, in which thin γ -MnO₂ sheets are grown on amorphous CoB alloy nano-chains (CoB@MnO₂), is produced via a simple and scalable solution-phase procedure at room temperature. A specific capacitance of 612.0 F g⁻¹ is obtained for the CoB@MnO₂ capacitor electrode at a discharge current density of 0.5 A g⁻¹, a value higher than those obtained for other conductive materials supported MnO₂ electrodes reported in the literature. A rate retention value of 60.9% of its initial capacitance is obtained when the discharge current density increased by 12-fold. It is found that after 6,000 charge-discharge cycles at 2 A g⁻¹, the specific performance of CoB@MnO₂ is 86.5%. The excellent capacitor performance of CoB@MnO₂ is explained to be due to the hierarchical core-shell structure in which the CoB alloy nano-chain backbone provides a transport pathway for the electron and the porous MnO₂ outer layers provide the channel for mass transfer and hence allowing further exposure to active sites. The combination of high capacitor performance and low-cost synthesis makes the core-shell CoB@MnO₂ a promising cathode material for alkaline electrolyte supercapacitors.

Keywords: CoB support; γ -MnO₂; Core-shell structure; Electrode; Supercapacitor.

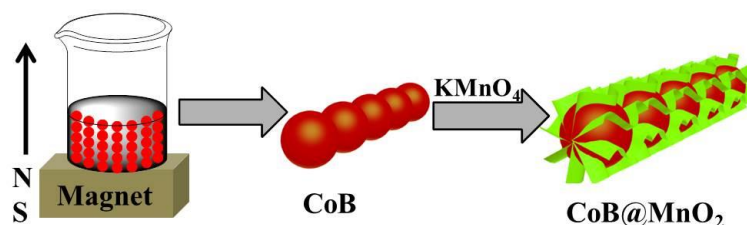
1. Introduction

Electrochemical capacitors (ECs) have attracted great interest in the energy storage sector owing to their high energy capability, reversibility, reliability and long cycling stability^{1, 2}. In an EC, the type of electrode material plays a key role for its performance and thus strenuous endeavor has been devoted to exploring various electrode materials. Among these materials, transition metal oxides such as RuO₂, MnO₂, Co₃O₄ and NiO, have been regarded as attractive and promising candidates due to the fact that they can provide highly efficient reversible redox charge transfer at various oxidation states, thus producing highly pseudo-capacitive behaviour³⁻⁶. Particularly, MnO₂ has been a research focus as it is low-cost, environmentally-friendly, abundant and possesses a fairly high theoretical electrochemical capacity⁷⁻¹². However, its actual energy storage capability is greatly restricted to around one fifth of its theoretical electrochemical capacitance mainly due to its intrinsically poor electrical conductivity ($\sim 10^{-5}$ S cm⁻¹)¹³.

To overcome the above issue, conductive reinforcers or additives have been introduced into the MnO₂ matrix to yield various hybrid materials for enhancing its capacitive abilities. According to the latest studies, there are four categories of additive conductive materials: the first consists of carbon materials, which are currently the most widely used additive conductive material. Various carbon materials such as carbon nanotubes (CNT), carbon fibers (CF), carbon paper and graphene have been mixed with manganese oxides and have shown increased capacitive properties to some extent compared to manganese oxide alone¹⁴⁻¹⁹. The second consists of

conductive polymers such as polyaniline (PANI), polypyrrol (PPY), and polythiophene (PTP). These conductive polymers have shown to offer good capacitance and high electronic conductivity, however they suffer from major limitations for practical applications due to their poor cycling stabilities and low mechanical stabilities²⁰⁻²². The third consists of metal. For example, when MnO₂ was incorporated into the three-dimensional porous Au, a high specific capacitance of ~ 601 F g⁻¹ at a current density of 0.5 A g⁻¹ was obtained as the electrodes provided fast ionic conduction and excellent electron-proton transport²³. Furthermore, these values were found to be much higher than those reported for hybrid materials made of MnO₂ and carbon materials^{16, 24}, conductive polymers^{22, 25}, and ternary composites^{26, 27}. However, the high price of Au metal inhibits its practical application.

Other reports have shown that metal hydrates, such as Ni(OH)₂, non-noble metals and alloys made of Ni, Co, TiN, can be incorporated into MnO₂ to improve the pseudo-capacitive performance of the EC electrodes^{23, 28-33}. These reports indicated that the EC electrode hybrid materials made of either metal or alloy conductive additives exhibited superior performances compared to those made of carbon materials and conductive polymers.



Scheme 1. Illustration of the formation of the hierarchical CoB@MnO₂ nanostructure.

In our previous work³⁴, CoB alloy was used as the support to *in-situ* grow porous

Ni(OH)₂ layers. It was found that the obtained hierarchical material exhibited high capacitive performance and cyclic stability, indicating that CoB alloys could be used as a conductive metallic additive. It was also found that other oxy/hydroxide hybrid capacitor electrode materials could lead to high specific capacitance and cycling stability. In this study, a hierarchical material made of MnO₂ layers and chain-like CoB alloy is designed and fabricated via a facile method with the objectives: (i) to expand on the use of CoB in ECs and (ii) to obtain high practical capacitance values. Firstly, a chain-like CoB alloy was synthesized via a reduction reaction under a magnetic field³⁴, as illustrated in Scheme 1. A subsequent uniform coating of a MnO₂ layer on the chain-like CoB surface was formed. It was observed that the reactions were easily generated on a large scale giving rise to well-constructed hybrid architectures.

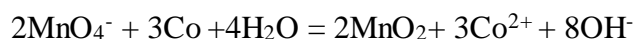
2. Experimental

2.1 Synthesis of CoB@MnO₂

All reagents were of analytic grade, and double-distilled water was used throughout the experiments. To prepare linear structured CoB sample, 0.35 mmol CoCl₂•6H₂O and 0.7 mmol NaOH were dissolved into 35 mL deionized water under stirring. Then 35 mL NaBH₄ (0.02 mol L⁻¹) solution was drop-wise added to the above solution with the fixed magnetic field intensity of ca. 0.4 Tesla. After reaction, the as-prepared CoB was rinsed with ultrapure water and ethanol alternately, and finally dried in vacuum oven at 40 °C for 8 h.

Subsequently, 20 mg of the as-prepared CoB was added into 20 mL deionized

water , and then 10 mL KMnO₄ (3 mM) was dissolved into the suspension. Then the suspension was operated mechanically at a rotation rate of 250 rpm for 0.5 h. The following reactions occurred:



After reaction, the product was rinsed with ultrapure water and ethanol alternately, and finally dried in vacuum oven at 40 °C for 8 h. The dried product was labelled as CoB@MnO₂.

2.2 Characterization

X-ray diffraction (XRD) patterns were recorded on a Shimadzu XD-3A (Japan) using filtered Cu-K α radiation ($\lambda = 0.15418$ nm) generated at 40 kV and 30 mA. Scans of 2θ values were recorded at 4° min⁻¹. Scanning electron microscopy (SEM) images were obtained using a Carl Zeiss Ultra Plus. Transmission electron microscopy (TEM) high angle annular dark field scanning transmission electron microscopy (STEM) images of the catalysts were obtained using a JEOL (JEM-2000 FX) microscope operating at 200 kV. Specific surface area was determined by Brunauer-Emmett-Teller (BET) method, and the density functional theory DFT method was employed for analyzing the full range of pore size distribution based on the sorption isotherms obtained on a Quantachrome Autosorb-1 volumetric analyzer. X-Ray Photoelectron Spectroscopy (XPS) spectra were generated using Thermo Scientific Escalab 250Xi. Binding energies were determined by referencing to the C 1s peak at 285.0 eV. The molar ratios of Co, B and Mn, in the bulk samples were

determined by a Varian 720 Inductively Coupled Plasma-Optical Emission Spectrometer (ICP-OES).

2.3 Electrochemical measurements

Cyclic voltammograms (CV) and galvanostatic charge/discharge tests on CoB@MnO₂ were carried out in a three-electrode cell system. The working electrode comprised a film of CoB@MnO₂, carbon black and poly(tetrafluoroethylene) with a mass ratio of 80:10:10, pressed into the Ni foam current collectors. A Hg/Hg₂SO₄ (saturated K₂SO₄) reference electrode and activated carbon counter electrode in 3.0 mol L⁻¹ LiOH electrolyte was used in all experiments. CV tests were carried out on a CHI 650D electrochemical workstation. Galvanostatic charge/discharge tests were carried out on a Neware Battery Tester (BTS6.0, Neware Technology Company, Guangdong, China).

The capacitance of the electrode (C) was calculated according to the following equation based on CVs or the discharge curves.

$$C = \frac{Q}{V} = \frac{i\Delta t}{\Delta V m} \quad (1)$$

Where i is the sampled current, Δt is a sampling time span, ΔV is the total potential deviation of the voltage window, and m is the mass of the active material examined.

3. Results and discussion

The obtained samples were firstly observed by scanning electron microscopy (SEM). As presented in Figure 1a, it can be seen that the chain-like CoB alloys are made of even bead-like particles. The magnified image in Figure 1b reveals a smooth and dense surface morphology of the bead-like particles of 50-250 nm in diameter.

The SEM image of CoB@MnO₂ in Figure 1c shows that the long chain skeleton is retained, and the chains assemble into bundles. The enlarged image in Figure 1d shows that the surface is covered by the formed continuous MnO₂ layer. This layer is made of many nano-chain surface cross-links, yielding the nano-chains to bundle together.

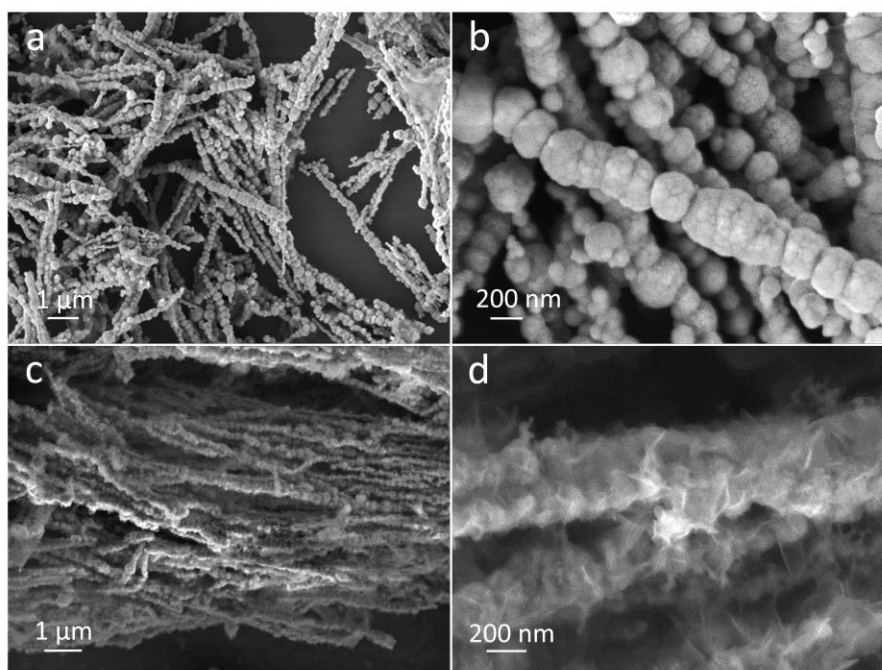


Figure 1. SEM images of (a,b) CoB and (c,d) CoB@MnO₂.

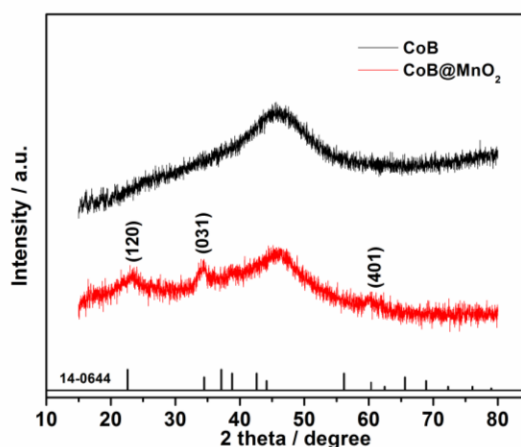


Figure 2. XRD patterns of CoB and CoB@MnO₂.

The crystalline structures of CoB and CoB@MnO₂ were characterized by X-ray

diffraction (XRD) as shown in Figure 2. It can be observed that a wide single peak arose at ca. 45° in the XRD pattern of CoB, confirming the amorphous structure of CoB. In the XRD pattern for CoB@MnO₂ and apart from the dispersion peak, three diffraction peaks at $2\theta \approx 23^\circ$, 34° and 60° were observed, corresponding to (120), (031) and (401) planes of the γ -MnO₂ phase (JCPDS 14-0644). However, these peaks are weak, indicating that the crystallinity of the *as*-prepared γ -MnO₂ is poor. Thus, the possibility of the existence of amorphous MnO₂ cannot be ruled out in the CoB@MnO₂ composite. The composition of the samples was determined by energy dispersive spectroscopy (EDS, Figure S1) and inductively coupled plasma (ICP). As shown in the figure, the signals for cobalt and boron appeared in the EDS patterns of CoB and CoB@MnO₂, and those related to manganese and oxygen arose in the EDS patterns of CoB@MnO₂. The bulk composition of the CoB@MnO₂ composite was analyzed by ICP. The Co:B:Mn atomic ratio in the composite was found to be ca. 23.9:13.3:1. The loaded mass content of MnO₂ on the CoB support was ca. 5.3 wt% of the total mass.

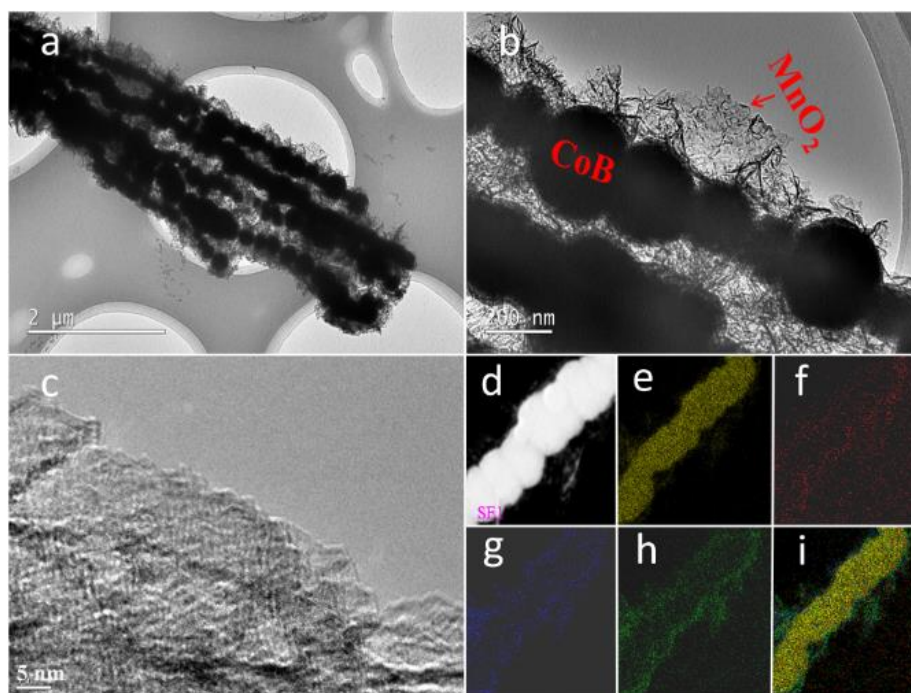


Figure 3. (a-c) TEM images of CoB@MnO₂ at various magnifications; (d) STEM of CoB@MnO₂; (e-h) elemental mapping of Co, B, Mn and O respectively; and (i) overlapped elemental mapping image of Co, B, Mn and O in CoB@MnO₂.

Transmission electron microscopy (TEM) was performed to reveal structural information of CoB@MnO₂. As shown in Figure 3a, a bunch of CoB@MnO₂ composed of chain-like cores and loose outer layers are clearly observed, which is consistent with SEM images. The enlarged image in Figure 3b indicates the presence of a flocculent layer covering the surface of the CoB nano-chain made of ultrathin sheets (ca. 5 nm in thickness). Furthermore, the pores shown in the irregular bright region can be observed by high-resolution TEM (Figure 3c), suggesting that the flocculent MnO₂ layer has a porous structure. To confirm this observation, N₂ isotherm analyses (Figure S2a) were carried out. The figure shows that the isotherm of CoB@MnO₂ presents an hysteresis loop, indicating a mesoporous structure for

CoB@MnO₂ and the mesopores were also confirmed by its pore size distribution (Figure S2b). It was also found that CoB@MnO₂ produces a much larger BET surface area of 50 m²g⁻¹ compared to that of CoB (6.6 m²g⁻¹). These findings further indicate that CoB@MnO₂ has a porous surface. In the selected area presented in the scanning TEM image (SETM, Figure 3d), an element distribution was performed by electron energy loss spectroscopy (EELS, Figure 3e-h). By overlapping the mappings (Figure 3i), it can be clearly observed that a hierarchical core-shell structure composed of a CoB alloy core and a MnO₂ shell was formed.

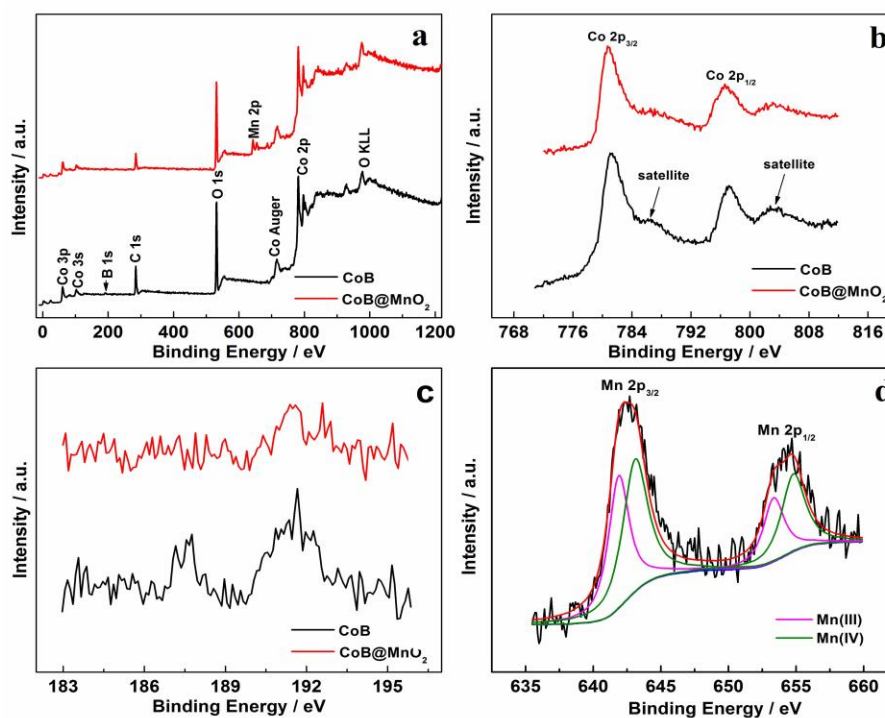


Figure 4. (a) Overall XPS surveys of CoB and CoB@MnO₂; (b) Co 2p; (c) B 1s XPS of CoB and CoB@MnO₂; (d) Mn 2p of CoB@MnO₂.

The constituent and chemical states of the samples' surfaces were evaluated by X-ray photoelectron spectroscopy (XPS). As shown in Figure 4a, the signals of Co

and B appeared in the two spectra, and the signal of Mn in the spectrum for CoB@MnO₂. The Co 2*p*_{1/2} and 2*p*_{3/2} peaks accompanied by the weak shake-up satellites appeared in the Co 2*p* XPS of the two samples (Figure 4b), suggesting that most of the Co atoms in the two samples presented a metal state^{35, 36}. This observation also implies the presence of the oxidation state of Co atom originating possibly from the electron transfer of Co→B which is further substantiated by the positive shift in binding energies (781.8 eV and 797.8 eV respectively) related to those of cobalt or its hydro/oxide forms^{36,37}. The obviously fading shake-up satellites in the Co 2*p* XPS of CoB@MnO₂ is possibly due to the suppressive effect of the MnO₂ signal on CoB. A similar phenomenon also occurred for the B 1*s* XPS signal. As shown in Figure 4c, the two obvious peaks at 191.6 eV and 187.5 eV, corresponding to the free pattern of B atoms and the presence of Co_xB alloy respectively³⁸, are observed in XPS of CoB, but these two peaks almost disappeared in CoB@MnO₂. In the case of Mn 2*p* XPS of CoB@MnO₂ (Figure 4d), the two peaks at 643.0 eV and 654.9 eV may be ascribed to Mn 2*p*_{3/2} and Mn 2*p*_{1/2} respectively. It was also found that the binding energies of Mn 2*p* from CoB@MnO₂ shifted positively compared to those from the bulk MnO_x³⁹⁻⁴¹. This is due to the fact that when MnO_x is highly dispersed on the support, a strong electrostatic field is produced, leading to the positive shift of the Mn 2*p* binding energy peak^{42,43}. The two pairs of doublets can be deconvoluted from the Mn 2*p* spectrum. The first pair of peaks at 641.9 and 653.3 eV can be assigned to Mn(III) atoms in the CoB@MnO₂ surface. The second doublet at higher bond energies (643.1 eV and 654.8 eV) correspond to Mn(IV)

atoms. By estimating the relative areas under the peak (integration), the Mn(III):Mn(IV) ratio on the surface was found to be ca. 4:5.

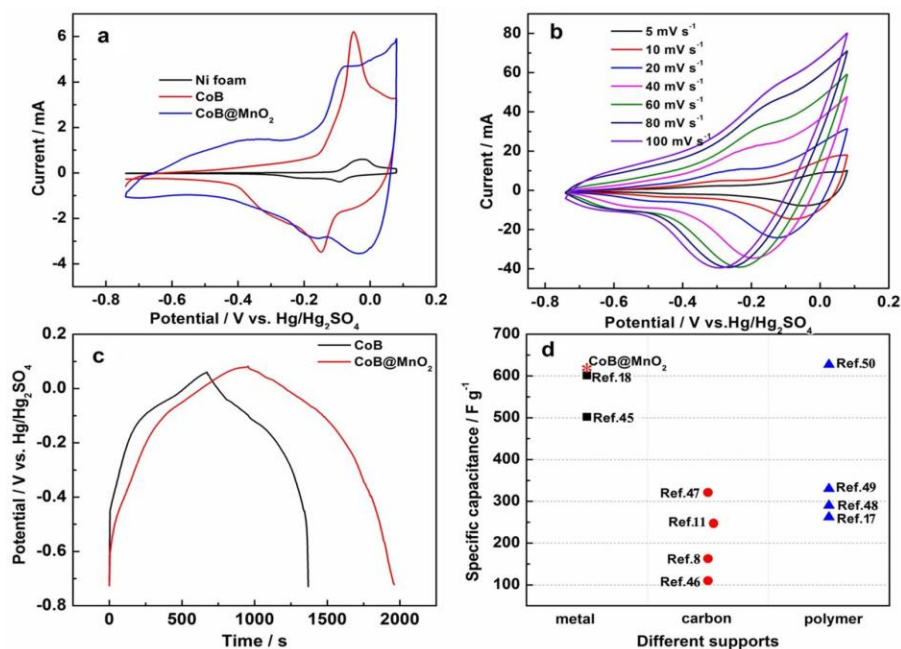


Figure 5. (a) Cyclic voltammograms of CoB@MnO₂, pure Ni foam, and CoB electrodes at a scan rate of 5 mV s⁻¹; (b) Cyclic voltammograms of CoB@MnO₂ at several scan rates; (c) galvanostatic charge-discharge curves of the CoB and CoB@MnO₂ electrodes at a current density of 0.5 A g⁻¹; (d) Comparison of the specific capacitance between CoB@MnO₂ and other conductive supports@MnO₂ core-shell-structured composites.

The capacitive behaviour of the obtained CoB@MnO₂ was evaluated by cyclic voltammetry (CV) and galvanostatic charge-discharge measured in a 3 mol L⁻¹ LiOH solution. For comparison purposes, a CV on a pure Ni foam electrode was conducted and used as the reference sample (Figure 5a). On the pure Ni foam electrode, two redox peaks (-0.033 V vs. Hg/Hg₂SO₄ and -0.091 V vs. Hg/Hg₂SO₄) were observed, which could be ascribed to the reversible conversion of the nickel oxide/hydroxide.

When CoB was loaded on the Ni foam electrode, the redox peaks appeared at more negative potentials i.e. at ca. -0.040 V vs. Hg/Hg₂SO₄ and -0.145 V vs. Hg/Hg₂SO₄ and the peak currents significantly increased compared to those of the pure Ni foam electrode, indicating that Co(OH)₂ was formed during the activation process through the oxidation reaction of Co^{34, 44, 45}. In the case of CoB@MnO₂, two features were observed. One was the double layer capacitive behaviour indicated by the presence of the double layer current in the low potential range, which mainly originated from the presence of MnO₂⁴⁶. The second was the pseudo-capacitive behaviour revealed via the large current from the clear redox peaks at high potentials, which was mainly due to CoB contribution. This finding suggests that the mixed capacitive behaviour could occur on the CoB@MnO₂ electrode during the charge-discharge process. In addition, the large area under the CV for CoB@MnO₂ indicates a charge storage ability of the material in comparison to that of CoB, suggesting that CoB@MnO₂ has better capacitance properties.

Cyclic voltammograms of CoB@MnO₂ at various scan rates ranging from 5 mV s⁻¹ to 100 mV s⁻¹ are shown in Figure 5b. It can be observed that the CVs generated at all scan rates are almost symmetrical. As the scan rate increases, the peak currents also increase with a negative potential shift while the CV shapes are nearly identical, suggesting the reversible ability of the fast charge-discharge process. Many studies have reported that the CVs on MnO₂ electrode immersed in a 3 mol L⁻¹ LiOH solution performed at high scan rates severely deviate from those at low scan rates (close to the ideal capacitive behaviour); this was found to be due to the sluggish electron

transfer and the incomplete intercalation of the electrolyte ions⁴⁷. Thus, it may be inferred that the increased and fast voltammetric response of CoB@MnO₂ compared to pure MnO₂ can be due to the presence of CoB. In our conditions, the good reversibility of CoB@MnO₂ at high scan rates could be attributed to the porous structure of the MnO₂ layer ensuring deep intercalation of the electrolyte ions together with the presence of CoB support boosting rapid electron transfer.

Figure 5c shows the galvanostatic charge-discharge plots of the CoB and CoB@MnO₂ electrodes from -0.72 V *vs.* Hg/Hg₂SO₄ to +0.08 V *vs.* Hg/Hg₂SO₄ at a current density of 2 A g⁻¹. The two plots shows non-linearity, a typical feature of pseudo-capacitance^{48,49}. From galvanostatic charge-discharge curves, it can be seen that the discharging regions for the two samples are almost symmetrical to their corresponding charging regions, suggesting high energy conversion efficiency. The specific capacitance value calculated from the discharge curve of the CoB@MnO₂ electrode was found to be 612.0 F g⁻¹, which is higher than that of the CoB electrode at 480.8 F g⁻¹. To further evidence the support effect of CoB, the specific capacitances of the reported core-shell composites comprised of other conductive materials are plotted in Figure 5d. The detailed comparative information is tabulated in Table S1. As observed, the reported specific capacitances for metal@MnO₂^{23, 50}, carbon materials@MnO₂^{13, 16, 51, 52} and most of polymer conductive materials@MnO₂^{22, 53, 54} are smaller than that of CoB@MnO₂, which is also in good agreement to the value reported in Ref.⁵⁵. This finding indicates that the charge energy capability of CoB@MnO₂ is attractive, which could be attributed to the conductive CoB support

servicing as the backbone for the MnO₂ surface layer.

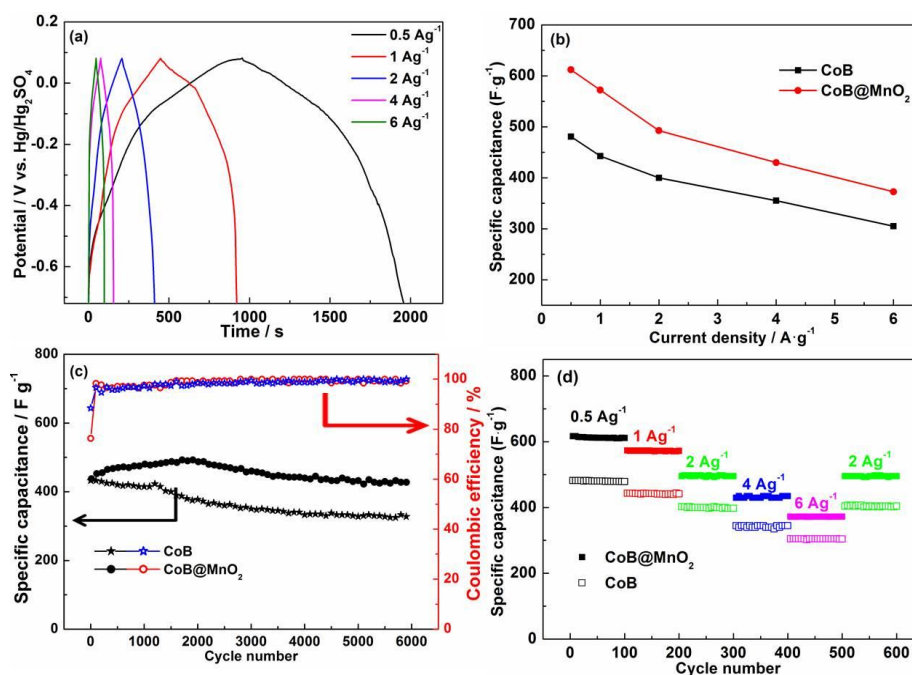


Figure 6. (a) Galvanostatic charge-discharge curves of the CoB@MnO₂ electrode at several current densities of 0.5, 1, 2, 4, and 6 A g⁻¹; (b) Variation in specific capacitances at various current densities of the CoB and CoB@MnO₂ electrodes; (c) Cycling performance of the CoB and CoB@MnO₂ electrodes for 6,000 cycles at 2 A g⁻¹; and (d) **Cycling stability of CoB@MnO₂ and CoB at different current densities.**

The rate capability of CoB@MnO₂ was tested at several current densities ranging from 50 mA g⁻¹ to 6 A g⁻¹ (Figure 6a,b and Figure S3). As the current density increased, the specific capacitances for the two electrodes decreased, a similar finding previously observed on other core/MnO₂-shell based electrodes^{13, 16, 22, 23, 50-54}. At large current densities, the arrival of ions into the internal structure of the material is limited, leading to a rapid increase in charge transport resistance and in turn yielding a decrease in specific capacitance. The specific capacitance of CoB@MnO₂ dropped from 612.0 F g⁻¹ at 50 mA g⁻¹ to 372.5 F g⁻¹ at 6 A g⁻¹ corresponding to a 60.9% rate

retention of its initial capacitance. The specific capacitance of CoB reduced from 480.8 F g⁻¹ to 305.1 F g⁻¹, corresponding to a 63.4% capacitance retention. Although the capacitance retention of the core-shell CoB@MnO₂ material was lower than that of CoB, the specific capacitance was much higher than that of CoB within the entire current density range. In addition, the specific capacitance of CoB@MnO₂ at 6 A g⁻¹ was 1.3 times higher than that of CoB. To further illustrate the good rate capability of CoB@MnO₂ (Figure S4), the specific capacitance of CoB@MnO₂ was 372.3 F g⁻¹ at a scan rate of 5 mV s⁻¹. When the scan rate increases to 100 mV s⁻¹, the specific capacitance for CoB@MnO₂ still remains 179.6 F g⁻¹, displaying its good rate capability.

The long-term cycling life of CoB@MnO₂ and CoB was tested over 6,000 continuous charge-discharge cycles at a current density of 2 A g⁻¹ (Figure 6c). After 6,000 cycles, it was observed that the loss of the specific capacitance of CoB@MnO₂ was 13.5%, whereas 24.3% specific capacitance was lost for CoB. Compared to the stability of other conductive core/MnO₂-shell based electrodes^{13, 16, 22, 23, 50-54}, the long-term cycling life of both CoB@MnO₂ and CoB were good (Figure 6c). It was also found that ca. 98% coulombic efficiency was maintained for both materials, suggesting efficient charge-discharge symmetries. In addition, the durability of the two materials was evaluated by the charge-discharge cycles at increased current densities (Figure 6d). As shown in the figure, during the cycles at several current densities, the loss in the specific capacitance was only ca. 0.2-0.8% after each 100 cycles. As the current density returned to 2 A g⁻¹, the capacitance of CoB@MnO₂ was

495 A g⁻¹, i.e. ~99.5% of the initial capacitance at 497 A g⁻¹ after 500 charge-discharge cycles. Moreover, this capacitance remained stable in the next 100 cycles. This finding suggests that CoB@MnO₂ could be possibly used for practical energy storage devices as the material exhibits good durability at various current densities.

The above results also indicate that CoB@MnO₂ composite has superior capacitance performance, which may be ascribed to its three unique physical properties. Firstly, the well-separated MnO₂ nano-flakes *in-situ* grown upon chain-like CoB backbone surface provide easy access for the absorption/desorption on the surface and intercalation/deintercalation of ions. Secondly, as shown in Figure 5a, Co(OH)₂ forms on the CoB surface when the electrolyte reaches the CoB core surface through the mesoporous channel in the MnO₂ flakes during activation in alkaline solution. Thus, Co(OH)₂ is involved (through the redox reaction) since mesopores in MnO₂ may allow electrolyte ions access, and in turns contributing to an enhanced specific capacitance of CoB@MnO₂. Thirdly, CoB provides a highly conductive support in CoB@MnO₂ for fast electron transport.

4. Conclusions

A hierarchically core-shell structured amorphous CoB alloy nano-chains@thin γ -MnO₂ sheets composite was produced via a simple solution-phase approach at room temperature. The constructed hierarchical CoB@MnO₂ as the electrode for pseudo-capacitors exhibited a high specific capacitance of 612.0 F g⁻¹ at a current density of 0.5 A g⁻¹, a high rate capacity of 60.9% of its initial capacitance when the

discharge current density increased by 12-fold, and an excellent cycling stability (86.5% specific performance remained over 6,000 charge-discharge cycles at 2 A g⁻¹). The excellent capacitor performance of CoB@MnO₂ was attributed to the unique hierarchically core-shell structure. It was found that: (i) the short ion diffusion pathways provided by a porous MnO₂ layer allowed fast and reversible charge-discharge behaviour; (ii) the one-dimensional CoB nano-chain core acted as an efficient conductive carrier; (iii) the close contact between CoB and MnO₂ allowed possible synergistic effects to improve the electrochemical performance. The overall performance and low-cost synthesis of the core-shell CoB@MnO₂ material makes it a very promising electrode for high-performance energy storage devices.

Acknowledgements

The authors would like to thank the National Natural Science Foundation of China (21363022 and 51661008) for financially supporting this work.

Author Contributions

Jingjing Yan and Hui Wang contributed to this work equally.

References

1. Y. Q. Zhang, L. Li, S. J. Shi, Q. Q. Xiong, X. Y. Zhao, X. L. Wang, C. D. Gu and J. P. Tu, *J Power Sources*, 2014, **256**, 200-205.
2. Y. Du, X. Zhao, Z. Huang, Y. Li and Q. Zhang, *RSC Adv*, 2014, **4**, 39087-39094.
3. J. Liu, J. Jiang, C. Cheng, H. Li, J. Zhang, H. Gong and H. J. Fan, *Adv Mater*, 2011, **23**, 2076-2081.
4. H. Jiang, C. Li, T. Sun and J. Ma, *Chem Commun*, 2012, **48**, 2606.
5. Y.-B. He, G.-R. Li, Z.-L. Wang, C.-Y. Su and Y.-X. Tong, *Energ Environ Sci*, 2011, **4**, 1288.
6. Q. Li, Z. L. Wang, G. R. Li, R. Guo, L. X. Ding and Y. X. Tong, *Nano Lett*, 2012, **12**, 3803-3807.
7. W. Wei, X. Cui, W. Chen and D. G. Ivey, *Chem Soc Rev*, 2011, **40**, 1697-1721.
8. X. Wang, S. Huo, R. Wang, H. Wang, D. J. L. Brett and S. Ji, *J Colloid Interf Sci*, 2017, **503**, 76-85.
9. J. Yang, H. Wang and R. Wang, *J Mater Sci-Mater El*, 2017, **28**, 6481-6487.

10. Q. Liu, S. Ji, J. Yang, H. Wang, B. G. Pollet and R. Wang, *Mater*, 2017, **10**.
11. L. Wang and H. Wang, *Micro Nano Lett*, 2017, **12**, 670-674.
12. Q. Liu, J. Yang, R. Wang, H. Wang and S. Ji, *Rsc Adv*, 2017, **7**, 33635-33641.
13. T. T. Lee, J. R. Hong, W. C. Lin, C. C. Hu, P. W. Wu and Y. Y. Li, *J Electrochem Soc*, 2014, **161**, H598-H605.
14. M. Liu, L. Gan, W. Xiong, Z. Xu, D. Zhu and L. Chen, *J Mater Chem A*, 2014, **2**, 2555.
15. J. W. Long, M. B. Sassin, A. E. Fischer, R. R. Debra, A. N. Mansour, V. S. Johnson, P. E. Stallworth and S. G. Greenbaum, *J Phys Chem C*, 2009, **113**, 17595-17598.
16. Y. Zhao, Y. Meng and P. Jiang, *J Power Sources*, 2014, **259**, 219-226.
17. T-T. Lee, J-R. Hong, W-C. Lin, C-C. Hu, P-W. Wu and Y-Y. Li, *J Electrochem Soc*, 2014, **161**, H598-H605.
18. T. Zhai, F. Wang, M. Yu, S. Xie, C. Liang, C. Li, F. Xiao, R. Tang, Q. Wu, X. Lu and Y. Tong, *Nanoscale*, 2013, **5**, 6790-6796.
19. Y. Qiu, P. Xu, B. Guo, Z. Cheng, H. Fan, M. Yang, X. Yang and J. Li, *RSC Adv*, 2014, **4**, 64187-64192.
20. G. Wang, L. Zhang and J. Zhang, *Chem Soc Rev*, 2012, **41**, 797-828.
21. Jaidev, R. I. Jafri, A. K. Mishra and S. Ramaprabhu, *J Mater Chem*, 2011, **21**, 17601.
22. J-G. Wang, Y. Yang, Z-H. Huang and F. Kang, *J Power Sources*, 2012, **204**, 236-243.
23. X. Lang, A. Hirata, T. Fujita and M. Chen, *Nat Nanotech*, 2011, **6**, 232-236.
24. Y. K. Zhou, B. L. He, F. B. Zhang and H. L. Li, *J Solid State Electr*, 2004, **8**, 482-487.
25. L. Chen, L. J. Sun, F. Luan, Y. Liang, Y. Li and X. X. Liu, *J Power Sources*, 2010, **195**, 3742-3747.
26. Y. Hou, Y. Cheng, T. Hobson and J. Liu, *Nano Lett*, 2010, **10**, 2727-2733.
27. S-B. Yoon and K-B. Kim, *Electrochim Acta*, 2013, **106**, 135-142.
28. Q. Lu, M. W. Lattanzi, Y. Chen, X. Kou, W. Li, X. Fan, K. M. Unruh, J. G. Chen and J. Q. Xiao, *Angew Chem*, 2011, **123**, 6979-6982.
29. H. Yi, X. Chen, H. Wang and X. Wang, *Electrochim Acta*, 2014, **116**, 372-378.
30. J. Kang, A. Hirata, H. J. Qiu, L. Chen, X. Ge, T. Fujita and M. Chen, *Adv Mater*, 2014, **26**, 269-272.
31. L. Y. Chen, Y. Hou, J. L. Kang, A. Hirata, T. Fujita and M. W. Chen, *Adv Energ Mater*, 2013, **3**, 851-856.
32. W. Ni, B. Wang, J. Cheng, X. Li, Q. Guan, G. Gu and L. Huang, *Nanoscale*, 2014, **6**, 2618-2623.
33. X. Wang, R. Xu, R. Wang, H. Wang, D. J. Brett, B. G. Pollet and S. Ji, *Ionics*, 2017, **23**, 725-730.
34. H. Wang, J. Yan, R. Wang, S. Li, D. J. Brett, J. Key and S. Ji, *J Mater Chem A*, 2017.
35. H. Wang, Z. Zhang, Y. Yang, K. Wang, S. Ji, J. Key, Y. Ma and R. Wang, *J Solid State Electr*, 2015, **19**, 1727-1733.
36. X. T. Zhang, H. Wang, J. L. Key, V. Linkov, S. Ji, X. L. Wang, Z. Q. Lei and R. F. Wang, *J Electrochem Soc*, 2012, **159**, B270-B276.
37. W. Huang, Z. Zuo, P. Han, Z. Li and T. Zhao, *J Electron Spectrosc*, 2009, **173**, 88-95.
38. B. Crist, *Mountain View, CA*, 1999.
39. L. Zhong Zhao and V. Young, *J Electron Spectrosc*, 1984, **34**, 45-54.
40. V. Di Castro and G. Polzonetti, *J Electron Spectrosc*, 1989, **48**, 117-123.
41. J. van Elp, R. H. Potze, H. Eskes, R. Berger and G. A. Sawatzky, *Phys Rev B*, 1991, **44**, 1530-1537.
42. Y-F. Han, F. Chen, Z. Zhong, K. Ramesh, L. Chen and E. Widjaja, *The J Phys Chem B*, 2006, **110**,

- 24450-24456.
43. F. Kapteijn, A. D. Vanlangeveld, J. A. Moulijn, A. Andreini, M. A. Vuurman, A. M. Turek, J. M. Jehng and I. E. Wachs, *J Catal*, 1994, **150**, 94-104.
 44. L. Ma, H. Zhou, X. Shen, Q. Chen, G. Zhu and Z. Ji, *RSC Adv*, 2014, **4**, 53180-53187.
 45. C. Yuan, X. Zhang, L. Hou, L. Shen, D. Li, F. Zhang, C. Fan and J. Li, *J Mater Chem*, 2010, **20**, 10809.
 46. R. Wang, Y. Ma, H. Wang, J. Key, D. Brett, S. Ji, S. Yin and P. K. Shen, *J Mater Chem A*, 2016, **4**, 5390-5394.
 47. Q. Qu, P. Zhang, B. Wang, Y. Chen, S. Tian, Y. Wu and R. Holze, *J Phys. Chem. C*, 2009, **113**, 14020-14027.
 48. K. Wang, C. Zhao, S. Min and X. Qian, *Electrochim Acta*, 2015, **165**, 314-322.
 49. W. Sun, X. Rui, M. Ulaganathan, S. Madhavi and Q. Yan, *J Power Sources*, 2015, **295**, 323-328.
 50. J.-K. Chang, S.-H. Hsu, W.-T. Tsai and I. W. Sun, *J Power Sources*, 2008, **177**, 676-680.
 51. Z. Fan, J. Chen, M. Wang, K. Cui, H. Zhou and Y. Kuang, *Diam Relat Mater*, 2006, **15**, 1478-1483.
 52. S. Hong, S. Lee and U. Paik, *Electrochim Acta*, 2014, **141**, 39-44.
 53. X. Zhang, W. Yang and Y. Ma, *Electrochem Solid-State Lett*, 2009, **12**, A95.
 54. X. Zhang, L. Ji, S. Zhang and W. Yang, *J Power Sources*, 2007, **173**, 1017-1023.
 55. A. Sumboja, C. Y. Foo, J. Yan, C. Yan, R. K. Gupta and P. S. Lee, *J Mater Chem*, 2012, **22**, 23921.